Article

Structure

Structural Architecture of the Nucleosome Remodeler ISWI Determined from Cross-Linking, Mass Spectrometry, SAXS, and Modeling

Graphical Abstract

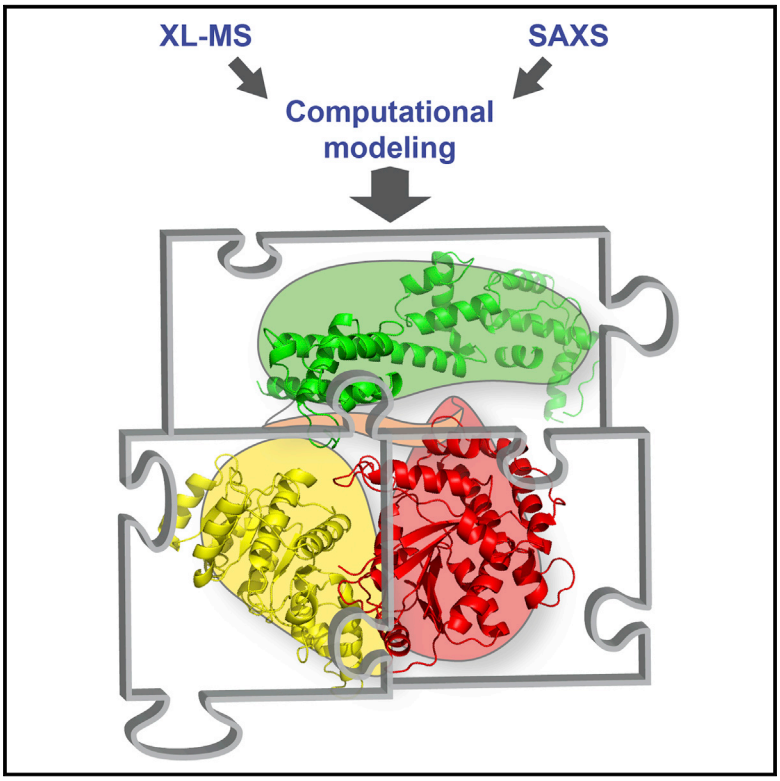

Highlights

- Full-length DmISWI structure revealed by XL-MS, SAXS, and computational modeling
- The two ATPase lobes are captured in a resting state in solution
- The flanking NTR and HSS domains pack against the ATPase core
- Large conformational changes are predicted upon binding to the nucleosome

Authors

Nadine Harrer, Christina E.M. Schindler, Linda K. Bruetzel, ..., Martin Zacharias, Jan Lipfert, Felix Mueller-Planitz

Correspondence

jan.lipfert@lmu.de (J.L.), fmueller@bmc.med.lmu.de (F.M.-P.)

In Brief

Harrer et al. reconstruct the conformation of the full-length ISWI chromatin remodeling enzyme in solution using an integrative structural approach. The model captures ISWI in the resting state and implies dramatic conformational changes upon binding to its nucleosome substrate.

Harrer et al., 2018, Structure *26*, 1–13
February 6, 2018
https://doi.org/10.1016/j.str.2017.12.015

CellPress

Please cite this article in press as: Harrer et al., Structural Architecture of the Nucleosome Remodeler ISWI Determined from Cross-Linking, Mass Spectrometry, SAXS, and Modeling, Structure (2017), https://doi.org/10.1016/j.str.2017.12.015

Structure
Article

Structural Architecture of the Nucleosome Remodeler ISWI Determined from Cross-Linking, Mass Spectrometry, SAXS, and Modeling

Nadine Harrer,[1] Christina E.M. Schindler,[2,4] Linda K. Bruetzel,[3] Ignasi Forné,[1] Johanna Ludwigsen,[1] Axel Imhof,[1] Martin Zacharias,[2,4] Jan Lipfert,[3,*] and Felix Mueller-Planitz[1,5,*]
[1]Molecular Biology, Biomedical Center, Faculty of Medicine, LMU Munich, 82152 Martinsried, Germany
[2]Physics Department (T38), Technical University of Munich, 85748 Garching, Germany
[3]Department of Physics, Nanosystems Initiative Munich, and Center for Nanoscience, LMU Munich, 80799 Munich, Germany
[4]Center for Integrated Protein Science Munich, 81377 Munich, Germany
[5]Lead Contact
*Correspondence: jan.lipfert@lmu.de (J.L.), fmueller@bmc.med.lmu.de (F.M.-P.)
https://doi.org/10.1016/j.str.2017.12.015

SUMMARY

Chromatin remodeling factors assume critical roles by regulating access to nucleosomal DNA. To determine the architecture of the *Drosophila* ISWI remodeling enzyme, we developed an integrative structural approach that combines protein cross-linking, mass spectrometry, small-angle X-ray scattering, and computational modeling. The resulting structural model shows the ATPase module in a resting state with both ATPase lobes twisted against each other, providing support for a conformation that was recently trapped by crystallography. The autoinhibiting NegC region does not protrude from the ATPase module as suggested previously. The regulatory NTR domain is located near both ATPase lobes. The full-length enzyme is flexible and can adopt a compact structure in solution with the C-terminal HSS domain packing against the ATPase module. Our data imply a series of conformational changes upon activation of the enzyme and illustrate how the NTR, NegC, and HSS domains contribute to regulation of the ATPase module.

INTRODUCTION

Nucleosomes organize and compact the genetic material. They are composed of ~150 bp of DNA that wraps around an octamer of histone proteins (Luger et al., 1997). The wrapped DNA is not accessible to most DNA-binding factors, a feature that cells use to regulate their genome. A specialized machinery deposits or dismantles nucleosomes, incorporates or exchanges histones and special histone variants, or moves entire nucleosomes to other locations in the genome. All these reactions are catalyzed by a family of molecular machines termed nucleosome remodeling enzymes (Swygert and Peterson, 2014). Given the diversity of activities, remodeling enzymes adopt central roles in all nuclear processes, and a growing list of malignancies is linked to this important class of enzymes (Garraway and Lander, 2013; Kadoch and Crabtree, 2015).

All nucleosome remodeling enzymes contain an ATPase motor domain from the Snf2 family of ATPases that is evolutionarily related to superfamily 2 DNA/RNA helicases and consists of two RecA-like lobes (Singleton et al., 2007). The ATPase domain harbors six important helicase-related sequence motifs (Flaus et al., 2006). Motifs I and II on lobe 1 assist in binding ATP and Mg^{2+}. These two motifs work cooperatively with motif VI on the second ATPase lobe, which acts as an "arginine finger" to assist catalysis (Durr et al., 2006). Both lobes therefore must align before the ATPase domain becomes competent to hydrolyze ATP.

Available structures of Snf2 ATPase domains differ drastically in the relative orientations of both ATPase lobes (Figure 1) (Durr et al., 2005; Hauk et al., 2010; Thoma et al., 2005; Xia et al., 2016; Yan et al., 2016). In most Snf2 ATPase structures, motifs I, II, and VI are not properly aligned, suggesting that the enzymes were crystallized in catalytically inactive states. It remains unclear whether the crystallized conformations are significantly populated in solution and whether they represent important regulatory states or intermediates during the nucleosome sliding reaction.

Remarkably, the ATPase domain itself contains much of the functionality of remodeling enzymes. The ATPase modules of Imitation SWI (ISWI) and Chd1, for instance, can bind the nucleosome core around superhelical location 2 (SHL2) and can remodel nucleosomes without the help of other domains (Dang and Bartholomew, 2007; McKnight et al., 2011; Mueller-Planitz et al., 2013b; Saha et al., 2005; Schwanbeck et al., 2004; Zofall et al., 2006).

Nevertheless, all remodeling enzymes possess a variety of accessory domains and subunits that carry out remodeler-specific functions (Mueller-Planitz et al., 2013a; Zhou et al., 2016). Some simply allow the remodeler to localize correctly along the genome. Others directly interfere with catalysis by steering the reaction toward reaction products that are characteristic of each remodeler. ISWI remodeling enzymes contain a C-terminal HAND-SANT-SLIDE (HSS) domain, which can associate with DNA that flanks the nucleosome (Dang and Bartholomew, 2007; Grune et al., 2003; Hota et al., 2013). The HSS domain releases from the flanking DNA in a nucleotide-state dependent

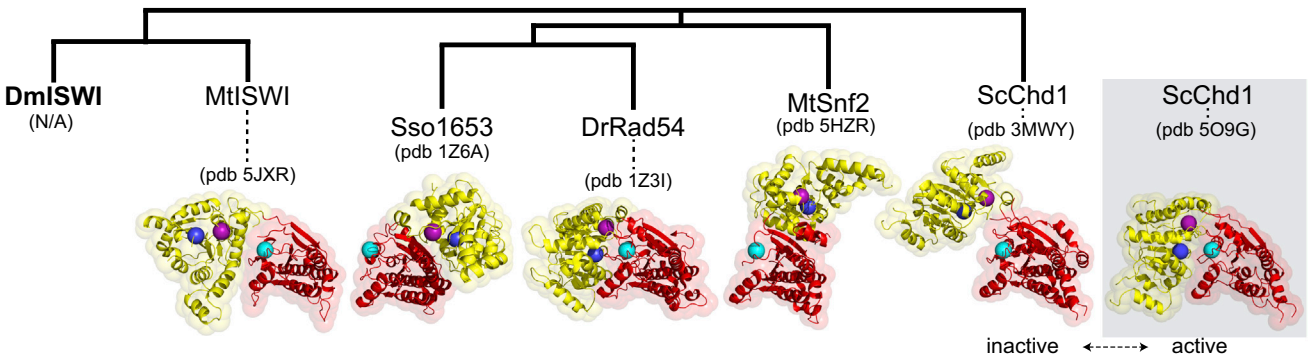

Figure 1. Available apo Structures of Snf2 Enzymes Differ in the Relative Orientations of Both ATPase Lobes

Phylogenetic tree of crystallized Snf2-type ATPase domains (PDB codes in brackets) and their evolutionary relationship to DmISWI. All structures are aligned to ATPase lobe 2 (red). The orientation of lobe 1 (yellow) drastically varies. Spheres indicate the positions of motifs involved in ATP hydrolysis (purple, motif I; blue, motif II; cyan, motif VI). The structure of ScChd1 in the catalytically competent state (Farnung et al., 2017) is shown for comparison (gray box). N/A, structure not available; Dm, *Drosophila melanogaster*; Mt, *Myceliophthora thermophila*; Sso, *Sulfolobus solfataricus*; Dr, *Danio rerio*; Sc, *Saccharomyces cerevisiae*.

manner, and, after undergoing a major conformational change, then interacts with the core of the nucleosome. This conformational change has been suggested to allow ISWI to measure the length of the flanking DNA (Leonard and Narlikar, 2015), which may be necessary to even out the spacing between nucleosomes in nucleosome arrays (Lieleg et al., 2015; Yang et al., 2006).

ISWI possesses additional domains that fulfill autoregulatory functions. The N-terminal region (NTR) for example inhibits the ATPase activity *in cis*. Binding of the H4 tail of the nucleosome near the NTR-ATPase interface releases this inhibition (Clapier and Cairns, 2012; Ludwigsen et al., 2017; Yan et al., 2016). Another regulatory region termed NegC is located at the C-terminal end of the ATPase domain. Like the NTR, it autoinhibits the enzyme (Clapier and Cairns, 2012).

Two very different conformations of NegC have been crystallized. NegC of ISWI from the thermophilic yeast *Myceliophthora thermophila* (MtISWI) protrudes from the globular ATPase domain and interacts with a neighboring protomer in the crystal (Yan et al., 2016). In Chd1 from *Saccharomyces cerevisiae* (ScChd1), the corresponding "brace-bridge" segment, for simplicity also termed NegC herein, packs against both ATPase lobes on the same protomer (Hauk et al., 2010).

ISWI represents an important model enzyme to study the mechanism of remodeling (Mueller-Planitz et al., 2013a; Narlikar et al., 2013). Unfortunately, no atomistic structural model of full-length ISWI is available to date, severely limiting our current understanding of the remodeling process. Nevertheless, high-resolution structural information exists for several individual domains. The structures of the HSS domains of *Drosophila melanogaster* ISWI (DmISWI) and Sc Isw1 have been solved (Grune et al., 2003; Yamada et al., 2011), the latter also in the presence of DNA, and a structure of the catalytic core of MtISWI including the NTR became recently available (Yan et al., 2016). However, the overall architecture of full-length ISWI (i.e., how the individual domains connect to each other) remains unknown.

In this study, we developed an integrated structural approach to investigate the conformation and conformational changes of the ATPase lobes in solution and to reconstruct the overall three-dimensional domain architecture of DmISWI. Our approach combines information from several structural techniques with computational modeling. Protein cross-linking followed by high-accuracy mass spectrometry (XL-MS) and small-angle X-ray scattering (SAXS) provided structural information about DmISWI and its domains, which we used to orient individual domains relative to each other and to model the overall solution structure.

Our results show a compact conformation of the ISWI protein with its HSS domain in close proximity to the ATPase module. Major structural rearrangements are necessary to reach the predicted extended conformation in the length-sensing state, in which the HSS and ATPase modules are bound at the same time to flanking DNA and the core of the nucleosome, respectively. The NTR domain was trapped near the interface of the ATPase lobes. Unexpectedly, it was proximal to the C-terminal end of ISWI, the SLIDE domain, which may allow crosstalk between these two important regulatory domains. The ATPase module rested in an inactive configuration that was remarkably similar to the structural state of MtISWI, which was recently crystallized (Yan et al., 2016), providing in solution evidence for this particular conformation. Our data do not support, however, NegC protruding away from the ATPase module and embracing a neighboring protomer as seen in the crystal. A Chd1-like conformation of NegC, on the other hand, is consistent with our data. More generally, our results demonstrate the power and usefulness of combining information from several solution-based techniques with computational modeling to gain structural insights when higher resolution techniques prove difficult to be applied.

RESULTS

Although structural models of individual domains exist, there is currently no full-length structure of ISWI available. Even the conformation of its ATPase domain remains unclear as structures of related ATPases differ drastically in the orientation of both ATPase lobes (Figure 1). To study the domain architecture of DmISWI, we developed an integrative process that combined data from XL-MS and SAXS with computational modeling (Figure 2A).

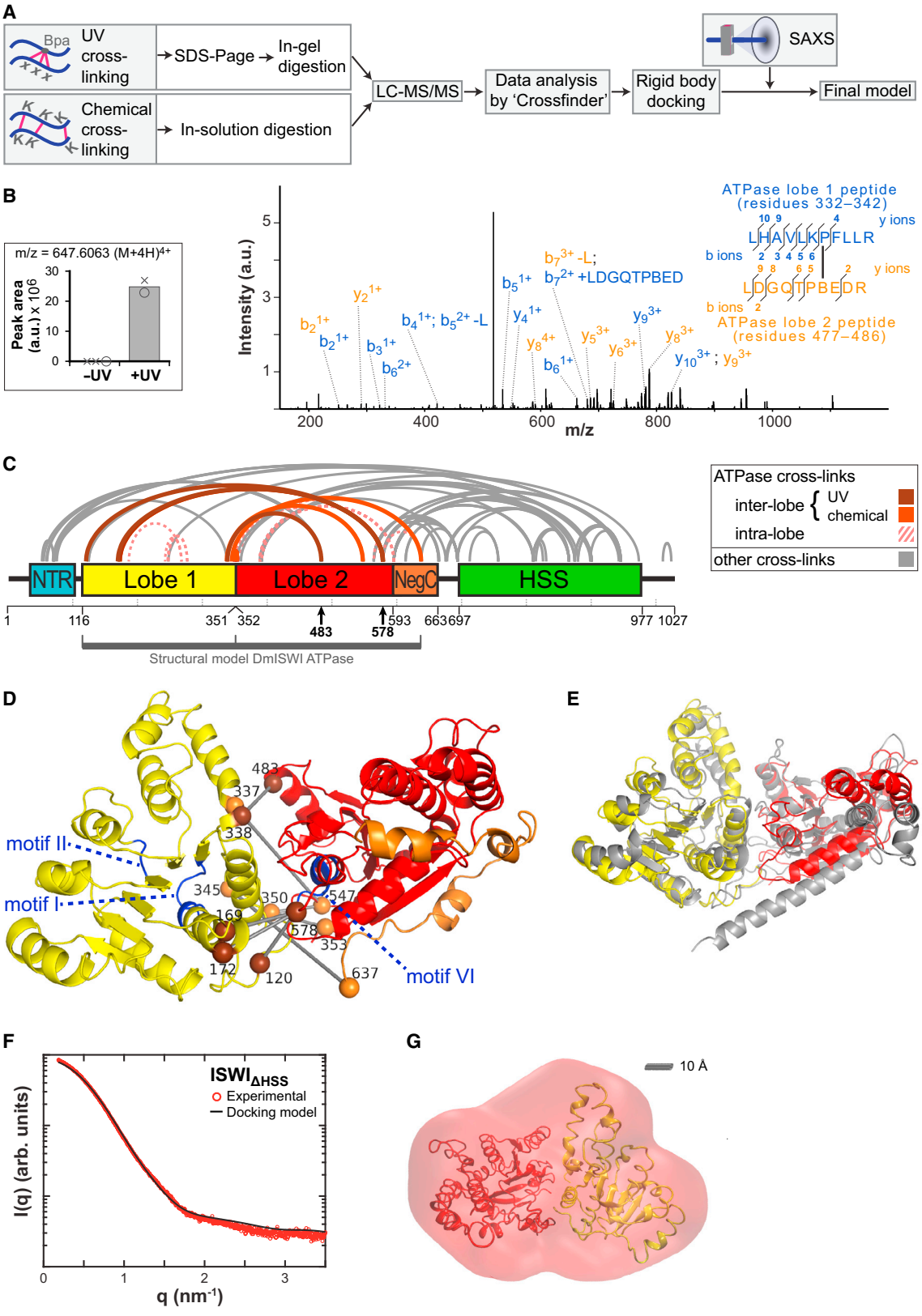

(legend on next page)

An XL-MS Approach to Study the ISWI Domain Topology

To guide structural modeling, we mapped protein cross-links in full-length DmISWI by MS. We employed two complementary cross-linking approaches. First, we chemically cross-linked lysine residues in wild-type DmISWI ($ISWI_{WT}$) with the homobifunctional cross-linkers BS^2G and BS^3. Second, we used the UV-inducible cross-linking amino acid *p*-benzoyl-*p*-phenylalanine (Bpa). We previously mapped several cross-links formed by Bpa that was site-specifically inserted into ATPase lobe 2 of full-length ISWI ($ISWI_{H483B}$ and $ISWI_{M578B}$) (Forné et al., 2012; Ludwigsen et al., 2017). Here we identified two additional cross-links for $ISWI_{M578B}$ (XL 7 and XL 48; Tables S1 and S2).

To identify cross-linked peptides in LC-MS/MS data, we used the software Crossfinder (Forné et al., 2012; Mueller-Planitz, 2015). Previously, Crossfinder was specialized to search for cross-links formed by site-specifically incorporated cross-linkers. We now extended Crossfinder's capabilities to also identify chemical cross-links. Crossfinder is optimized for high-resolution MS data. In total, we mapped 101 cross-linked peptides within DmISWI, which provided 68 nonredundant cross-link connections (Tables S1 and S2).

The ATPase Domain Assumes a Resting Conformation in Solution

Altogether, we mapped 37 cross-linked residues within the ATPase module (Table S1), which we define to include the NTR, ATPase lobe 1, ATPase lobe 2, and NegC domains. To deduce the structure of the ATPase module, we focused on the subset of cross-links that connected two domains in the module. XL 1–7 connect residues of both ATPase lobes, and we first checked whether these cross-links were compatible with related high-resolution structures. None of the crystal structures of ScChd1, MtSnf2, DrRad54, and Sso1653 fitted all the distance restraints provided by XL 1–7 (Table 1). In contrast, all the distance restraints were satisfied in the recently determined structure of MtISWI. The configuration of MtISWI was also consistent with SAXS data of the DmISWI ATPase domain ($ISWI_{\Delta HSS}$). The predicted scattering profile of a homology model of MtISWI provided an excellent fit to the experimental data (χ = 0.71; Figure S3A). Except for ScChd1, other crystallized ATPase conformations fitted the SAXS data significantly worse (Figure S3A).

To independently probe the conformation of the ATPase, we next performed cross-link-constrained computational modeling. First, we built a homology model of the ATPase module from the structure of the remodeler ScChd1 (PDB: 3MWY), the most closely related remodeler with available structure when we began our study. This model comprised ATPase lobes 1 and 2 and large parts of NegC. We cut the homology model in the linker that connects both ATPase lobes, which yielded two structural bodies. The two lobes were then docked as rigid bodies using cross-links as structural guides by the ATTRACT engine (de Vries et al., 2015). Initially, we used only high-confidence cross-links that connected the two ATPase lobes (XL 1–3) as distance restraints during docking, disregarding lobe-lobe connecting cross-links with lower confidence (XL 4–7) and cross-links that mapped to regions outside of the homology model (XL 13–20, 30–37). Cross-links to NegC (XL 8–12) were not included during modeling due to potential flexibility (Clapier and Cairns, 2012); they were used during validation of the model instead (see below).

Cross-linking guided docking generated 200 structural models. These models shared an overall similar topology as indicated by a model precision of 3.4 Å (see STAR Methods). Compared with the initial ScChd1 conformation, lobe 1 was strongly rotated relative to lobe 2 in the models such that the catalytic motifs I and II no longer faced the interface between both lobes.

We screened the models against our SAXS data to identify the best-fitting model (Koch et al., 2003; Lipfert and Doniach, 2007; Putnam et al., 2007). The model with the lowest χ-fit was selected as a representative (Figure 2D), hereafter referred to as the DmISWI ATPase model. The selection is justified, as models with a similarly high level of agreement with the SAXS data are also structurally very close (Figure S2A).

We evaluated the quality and reliability of the DmISWI ATPase model with six approaches. First, we confirmed that the model satisfied the cross-linking distance restraints used during docking (XL 1–3; Table S1). Second, we tested whether cross-links that were not used during docking supported the model. All intra-lobe cross-links (XL 22–29) were consistent with the model, indicating a conserved fold of individual domains. Importantly, the model also explained additional interdomain cross-links, including lower-quality lobe-lobe cross-links and cross-links to NegC (XL 4–12). Of these cross-links, eight out of nine Cα-Cα distances agreed with our ATPase model (Table S1). Only XL 8 exceeded the allowed distance by ~5 Å. This cross-link, however, connects to the extreme C-terminal residue of the model

Figure 2. The ATPase of DmISWI Rests in an Inactive Conformation in Solution

(A) Workflow of our integrative structural approach.

(B) Validation of the UV cross-link XL 3 (Table S1). Left: Extracted ion chromatogram showing UV-dependent formation of the cross-link. Bar is average value of two independent measurements shown in circles and crosses. Right: MS2 fragmentation spectrum with assigned product ions. B, Bpa.

(C) Schematic representation of DmISWI domains with experimentally determined cross-links indicated as arcs. Amino acid numbers are provided underneath. UV (brown) and chemical (orange) cross-links connecting both ATPase lobes are represented by solid arcs, intra-domain cross-links by dotted arcs. Arrows indicate Bpa positions.

(D) Structural model of the ATPase domain of DmISWI (residues 116–637; colors as in C). Brown and orange spheres mark amino acids involved in UV and chemical cross-linking, respectively; rods represent cross-links. Catalytic motifs are colored blue. Table S1 lists distances spanned by the cross-links.

(E) Superposition of the model in (D) with the MtISWI crystal structure (gray; PDB: 5JXR; the NTR and NegC regions were omitted for clarity). RMSD = 4.5 Å.

(F) Experimental scattering profile for $ISWI_{\Delta HSS}$ (red circles). The theoretical SAXS curve (black line) from the model in (D) is in good agreement with the data (χ = 1.03).

(G) SAXS envelope reconstruction of $ISWI_{\Delta HSS}$ fitted with the DmISWI ATPase model shown in (D); 19% of residues are missing in the model, explaining excess electron density.

See also Figures S2 and S3 and Table S1.

Table 1. Interdomain Cross-Links in the ATPase of DmISWI and Related Crystal Structures

	DmISWI (Cross-Links)			ScChd1 (PDB: 3MWY)			Sso1653 (PDB: 1Z6A)			DrRad54 (PDB: 1Z3I)			MtSnf2 (PDB: 5HZR)			MtISWI (PDB: 5JXR)		
	Site[a]		Cα-Cα	Site		Cα-Cα	Site		Cα-Cα	Site		Cα-Cα	Site		Cα-Cα	Site		Cα-Cα
XL	1	2	Threshold (Å)	1	2	Distance (Å)[b]	1	2	Distance (Å)[b]	1	2	Distance (Å)[b]	1	2	Distance (Å)[b]	1	2	Distance (Å)[b]
1	578	172	≤20	842	420	≥29.0**[c,d]	878	488	42.7**[c]	638	196	37.9**[c]	1020	598	NA	637	230	16.9
2	578	120	≤20	842	368	≥27.9**[c,d]	878	437	35.8**[c]	638	140	37.4**[c]	1020	546	NA	637	179	12.3
3	338	483	≤20	592	747	49.5**	644	784	53.0**	384	543	37.5**	776	865	56.4**	395	542	18.1
4	547	350	≤29	811	604	12.3	847	658	13.1	607	396	13.8	989	788	11.3	606	407	9.7
5	337	547	≤29	591	811	34.4**	643	847	33.5*	383	607	36.2**	775	989	36.3**	395	606	21.0
6	350	353	≤25	604	607	8.3	658	661	7.7	396	399	8.7	788	791	8.9	407	410	9.6
7	169	578	≤20	417	842	≥24.8*[d]	485	878	40.5**	193	638	33.4**	595	1020	NA	227	637	18.4
8	637	345	≤29	906	599	12.1	NA	651	NA	n/a	391	NA	NA	783	NA	705	402	51.2**
9	637	577	≤25	906	841	13.7	NA	877	NA	n/a	636	NA	NA	1019	NA	705	636	26.5*
10	637	356	≤25	906	610	17.0	NA	664	NA	n/a	402	NA	NA	794	NA	705	413	43.9**
11	391	595	≤25	645	862	≥2.1[d]	700	892	12.0	438	652	16.7	831	1036	NA	450	654	54.8**
12	388	595	≤25	642	862	NA	699	892	10.8	435	652	12.3	828	1036	NA	445	654	60.3**

NA, not available. Either the region surrounding the cross-link was not crystallized or no sequence homology to DmISWI exists.

[a]Amino acid numbering as in Figure 2C.

[b]Values marked with asterisks exceed distance restraints provided by DmISWI cross-links by ≤5 Å (*) and >5 Å (**).

[c]Calculated distances taken from Forné et al. (2012).

[d]ScChd1 Y842 and F645 are missing from the crystal structure. Lower limits were calculated from the distances to adjacent amino acids (Y841 or F646, respectively) minus the maximal distance between neighboring Cα atoms (3.9 Å).

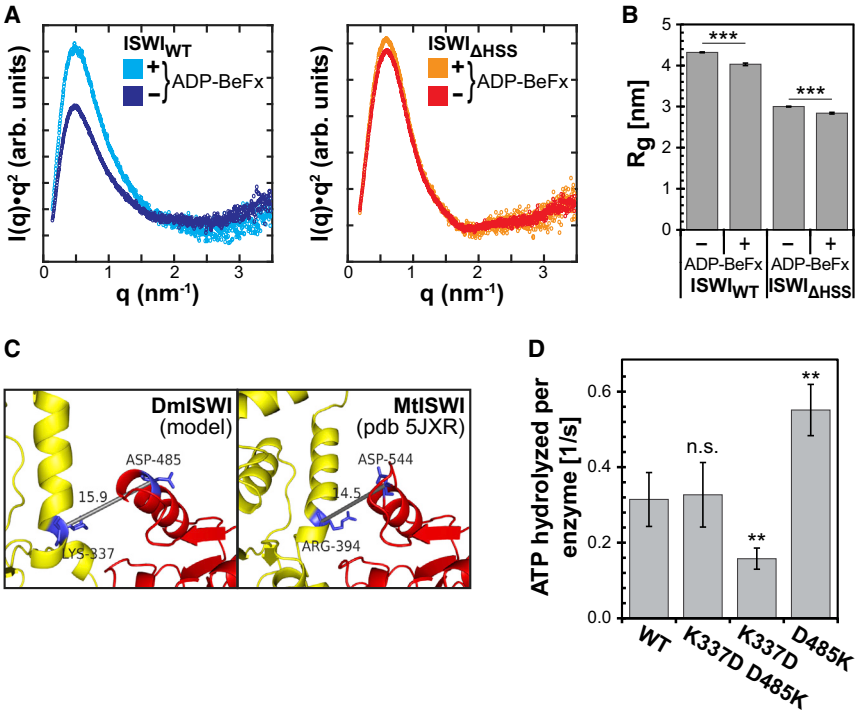

Figure 3. Conformational Changes in the ATPase Domain of ISWI Upon Activation

(A) Kratky representation of SAXS scattering profiles of ISWI$_{WT}$ and ISWI$_{\Delta HSS}$ in the presence and absence of the nucleotide analog ADP-BeF$_x$.

(B) Radii of gyration (R_g) derived for ISWI$_{WT}$ and ISWI$_{\Delta HSS}$ in the presence (+) or absence (–) of ADP-BeF$_x$. Data are represented as mean ± SD; a t test was performed to determine statistical significance. ***p ≤0.001.

(C) Potential inhibitory interaction between K337 in lobe 1 and D485 in lobe 2 in DmISWI (left) and corresponding residues in MtISWI (right).

(D) ATPase activities of ISWI$_{WT}$ and lobe interface mutants in the presence of saturating concentrations of ATP and DNA. Data are represented as average ± SD (n ≥3 independent measurements). The unstimulated basal activity was ≤0.005 s^{-1} for all enzyme variants. A two-tailed t test was performed to determine statistical significance. **p ≤0.01; n.s., not significant, p ≥0.05.

See also Figures S1 and S4.

(K637), which is located in a flexible region, providing an explanation for this discrepancy. Third, docking with all cross-links within the ATPase module yielded superimposable structures (root-mean-square deviation [RMSD] = 2.6 Å; Figure S3B).

Fourth, we checked our SAXS data of the ATPase module of ISWI (ISWI$_{\Delta HSS}$) for consistency with the model. SAXS confirmed that the protein is well folded, as indicated by a single pronounced peak in the Kratky representation ($I(q)q^2$ versus q; Figure 3A). The scattering data also were in good agreement with our ATPase model (χ = 1.03; Figure 2F), and the DmATPase model fitted well into the *ab initio* determined volume envelope determined from the SAXS data (Figure 2G). Extra density visible in the SAXS reconstruction is explained by the fact that our DmISWI ATPase model lacks 19% residues. Modeling of the missing residues using the software BUNCH improved the fit, but the placement of the missing loops appeared unphysical. We therefore did not pursue this approach further.

As a fifth validation of the model, we tested whether the docking procedure biased the structure into the modeled conformation by performing *ab initio* docking without cross-links. The *ab initio* model differed strongly from the DmISWI ATPase model (Figure S3C), and many lobe-lobe connecting cross-links were not satisfied (XL 1–3, 5, 7; not shown). The catalytic motif VI on lobe 2 now faced motifs I and II on lobe 1, suggesting a more active conformation. We conclude that the empirical force field used during docking did not bias the conformation toward the one seen in Figure 2D and suggest that the ATPase lobes inherently favor a state in which the conserved motifs I, II, and VI are in close proximity to one another.

As the sixth and last validation, we compared our DmATPase model with the recent MtISWI crystal structure, which became available after completion of our study. Superposition revealed a strikingly similar conformation (RMSD = 4.5 Å; Figure 2E). With the exception of NegC cross-links that we discuss separately below, all cross-links are largely consistent with the crystal structure (Table S1). Our solution data therefore provided strong independent support for the unexpected conformation seen in the crystal. Of note, our integrative structural approach predicted this conformation without prior knowledge of the crystal structure. In summary, all available data support the configuration of the ATPase module shown in Figure 2D. Nonetheless, we cannot rule out some degree of flexibility or a fraction of alternative conformations present.

The ATPase Module Undergoes a Major Conformational Change Upon Activation

Inspection of the DmATPase model shows that the enzyme is trapped in a resting state. Motif VI on lobe 2 and motifs I and II on lobe 1 were not oriented toward each other (Figure 2D), preventing productive ATP hydrolysis. We hypothesized that binding of the nucleotide analog Adenosine-5′-diphosphate beryllium-fluoride (ADP-BeF$_x$), which can mimic various nucleotide states including the transition state of the hydrolysis reaction (Farnung et al., 2017; Racki et al., 2014), forces alignment of motifs I, II, and VI.

Using SAXS, we sought to probe for a conformational change upon ADP-BeF$_x$ binding (Figure 3A). Binding of ADP-BeF$_x$ to ISWI$_{WT}$ and ISWI$_{\Delta HSS}$ decreased the radius of gyration (R_g), which is a measure of the compactness of a protein, by 7% and 5%, respectively (Figure 3B). These results suggest that the ATPase module undergoes a global conformational change upon nucleotide analog binding. We speculate that the nucleotide induces a rotation of the ATPase lobes to a more active conformation as seen in ADP-BeF$_x$-bound ScChd1 (Farnung et al., 2017), in which motifs I, II, and VI align to simultaneously contact the nucleotide.

To better pinpoint the location of the conformational change, we turned to mutagenesis. The model from Figure 2D predicts an interface between both lobes that may keep them locked in

the resting state. We sought to perturb this interface by introducing point mutations in K337 and D485 (Figures 3C and S4A) to test this possibility. We hypothesized that charge-reversal mutations (K337D or D485K) may weaken the interface. These mutations would stimulate ATP turnover in case this interface repeatedly forms and breaks during the hydrolysis cycle. In the simplest case, double mutation of both residues would then restore the stability of the interface and thereby the ATPase activity. Consistent with our hypothesis, mutation of D485K noticeably increased the ATPase activity compared with wild-type, and the double mutation restored wild-type ATPase levels (Figure 3D). $ISWI_{K337D}$ unexpectedly hydrolyzed ATP less robustly. It is possible that the negative charge introduced by the K337D mutation was stabilized by favorable interactions with basic residues on the other side of the interface, such as H483 or R486. Alternatively, given the high level of conservation of both ATPase lobes, it is plausible that K337 serves other critical functions in addition to stabilizing the interface and that its mutation leads to unexpected side effects. A more detailed structure-function analysis will be required to fully appreciate the function of the predicted interface.

In summary, our SAXS analysis points to a major reorientation of the ATPase module upon binding of nucleotides. We tentatively suggest that this reorientation involves breaking an interface between both lobes that keeps the enzyme in a resting state.

The C-Terminus of the HSS Domain Packs against the ATPase Domain

Having obtained a plausible model of the ATPase domain, we next modeled the HSS domain relative to the ATPase module. XL-MS of full-length DmISWI revealed 31 cross-linked amino acid pairs (XL 38–68; Table S2) that mapped to the HSS domain (Figure 4B), 15 of which connected the HSS with the ATPase domain (XL 38–52). These cross-links spanned hundreds of amino acid residues in the primary sequence, consistent with a compact structure formed by the HSS and ATPase modules.

With seven cross-links (XL 38, 41, 42, 44, 45, 46, 48), the SLIDE domain within the HSS module cross-linked particularly strongly to the ATPase domain, suggesting the existence of a previously unknown domain interface. Two complementary XL-MS approaches (chemical and photo cross-linking) provided independent evidence for spatial proximity of these domains. In contrast, the HAND domain did not cross-link to the ATPase domain. The eight lysine residues of the HAND domain are well distributed, and seven of them were accessible to the cross-linker as suggested by detection of mono-links, which form when the cross-linker reacts only with one of its two functional groups (data not shown). We therefore conclude that the HAND domain is solvent exposed but not part of the ATPase-HSS domain interface.

To model the interactions between the ATPase and HSS domain, we first selected the ten ATPase models that best fit our SAXS data. These ten structures formed an ensemble that we then docked against the crystal structure of the HSS domain. Docking was guided by the five high-confidence cross-links connecting the HSS to the ATPase domain (XL 38–42; Figures 4A and S5). All final 200 models showed convergence in the orientation of the ATPase to the HSS domain (precision = 3.3 Å; Figure S2B). The model with the lowest χ-fit to the SAXS data was selected as the representative full-length DmISWI model (Figures 4C and 4D; χ = 1.04), which is justified as models that achieve similar agreement with the SAXS data are also structurally very close to the representative conformation (Figure S2B). Reconstruction of the molecular envelope showed that the protein adopted a compact, folded shape, which well accommodated the structural model (Figure 4E). Excess density is explained by 22% missing residues in the model. As for $ISWI_{\Delta HSS}$ above, attempts to reconstruct these residues with BUNCH yielded physically implausible models.

To evaluate the full-length DmISWI model, we measured the distances between cross-linked residues (Table S2). The majority of ATPase-HSS cross-links are largely consistent with our model. Three cross-links (XL 44, 45, 47), however, violated the expected distance limit by more than 20 Å. When we included them and other lower confidence cross-links during docking, we obtained a similar structural configuration (Figure S6A), but again we could not model a single conformation that satisfied all cross-links. We also considered that the DmATPase model (Figure 2D) might not be optimal. We thus severed ATPase lobe 1 from lobe 2 and simultaneously docked both lobes against the HSS domain. The HSS domain docked in a similar fashion to the ATPase module, as observed for the two-body docking approach (Figure S6B). Several distance restraints were better satisfied by the resulting model (Tables S1 and S2). Also, the fit to the SAXS data modestly improved (χ = 0.85); however, XL 44, 45, and 47 were still not consistent with the structure. We therefore believe that flexibility in one or more parts of the protein prevents us from modeling a single configuration that can explain all XL-MS data. Indeed, ISWI contains several flexible domains, including the NTR, NegC, HSS, and the ATPase lobes, which all have been predicted to undergo conformational changes (Clapier and Cairns, 2012; Leonard and Narlikar, 2015; Lewis et al., 2008; Mueller-Planitz et al., 2013b). Whereas our experimental data are not sufficient to resolve all these conformations, we note that the interface between lobe 2 and the HSS domain is well constrained by our cross-linking and docking results.

It is well established that the HSS domain binds DNA (Dang and Bartholomew, 2007; Grune et al., 2003; Hota et al., 2013; Yamada et al., 2011). The DNA-binding site of the HSS is partially blocked in our structural model of DmISWI (Figure S6C). A blocked DNA-binding site on the HSS domain suggests that the enzyme is trapped in a resting state in the absence of substrate and that it undergoes a conformational change upon activation.

NegC Does Not Protrude from the Globular ATPase Domain

The enzymatic activity of ISWI is regulated by the NegC domain (Clapier and Cairns, 2012), but how regulation by NegC is achieved structurally is not clear. In the structure of ScChd1, NegC connects lobe 1 and lobe 2 and may thereby hold the enzyme in an inactive state (Hauk et al., 2010). In contrast, the NegC domain of MtISWI forms two helices that protrude from the globular ATPase domain and interact with a neighboring protomer in the crystal (Yan et al., 2016).

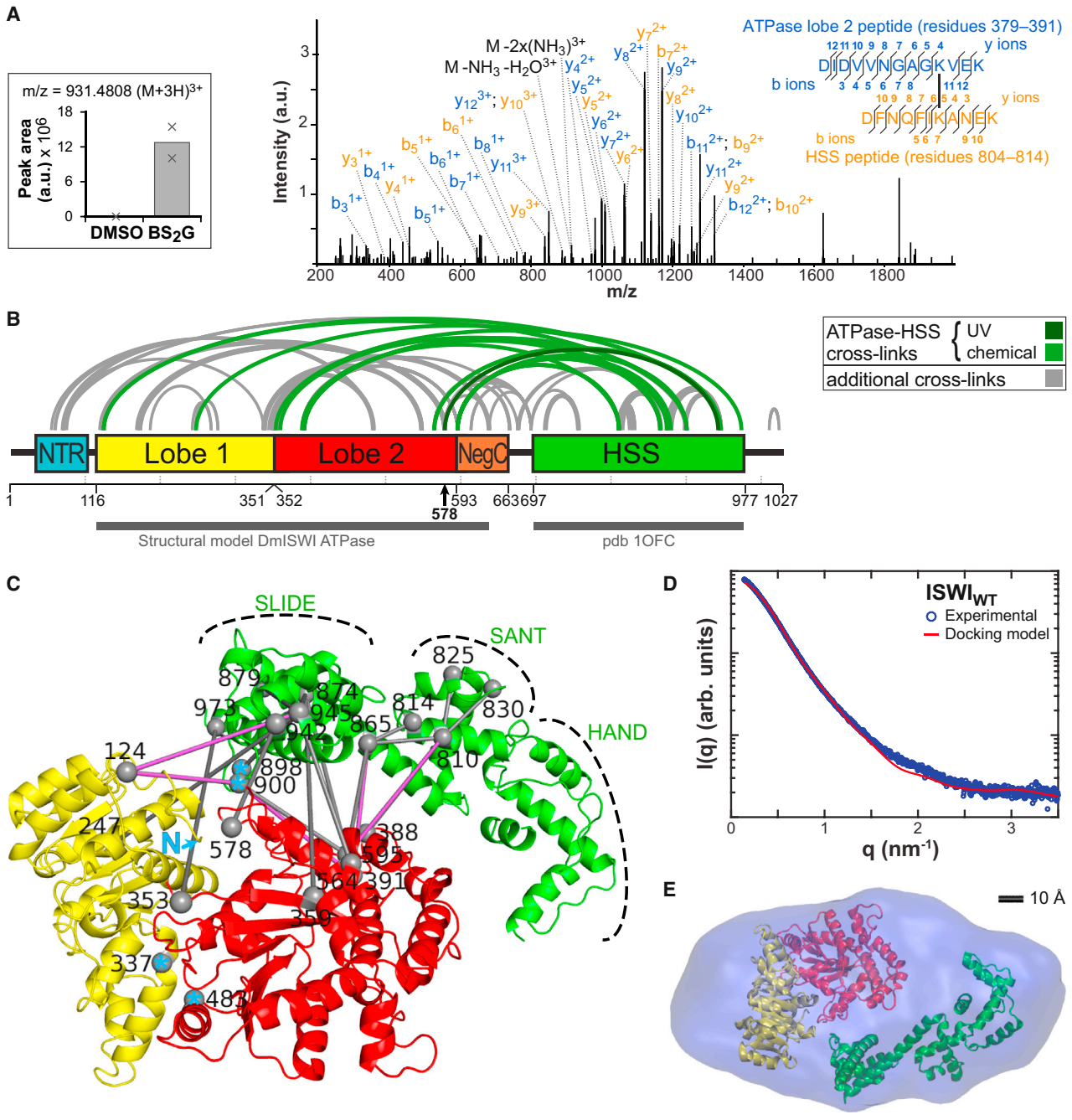

Figure 4. Interaction between the ATPase and HSS Domains of DmISWI

(A) Validation of a high-confidence chemical cross-link (XL 40; Table S2) formed between K388 and K810. Left: Extracted ion chromatogram. Bar is average value of two technical replicates (×). Right: MS2 fragmentation spectrum. See Figure S5 for additional high-confidence cross-links.

(B) Cross-links connecting the HSS and the ATPase domains (green).

(C) Structural model of DmISWI (residues 116–637 and 697–977). Rods indicate cross-links, whereby cross-links used for structural docking are colored pink. Cyan asterisks mark residues that cross-link to the NTR, which is not part of the model. N, N-terminal residue of the ATPase model. Distances spanned by the cross-links are summarized in Table S2.

(D) The experimental scattering profile for $ISWI_{WT}$ (blue circles) and the theoretical SAXS curve predicted from the ISWI full-length model in (C) (red line) are in good agreement (χ = 1.04).

(E) Reconstructed SAXS envelope of $ISWI_{WT}$ (residues 1–1027) fitted with our ISWI full-length model in (C). Extra density is largely explained by 22% missing residues of the model compared with $ISWI_{WT}$.

See also Figures S2, S5, and S6 and Table S2.

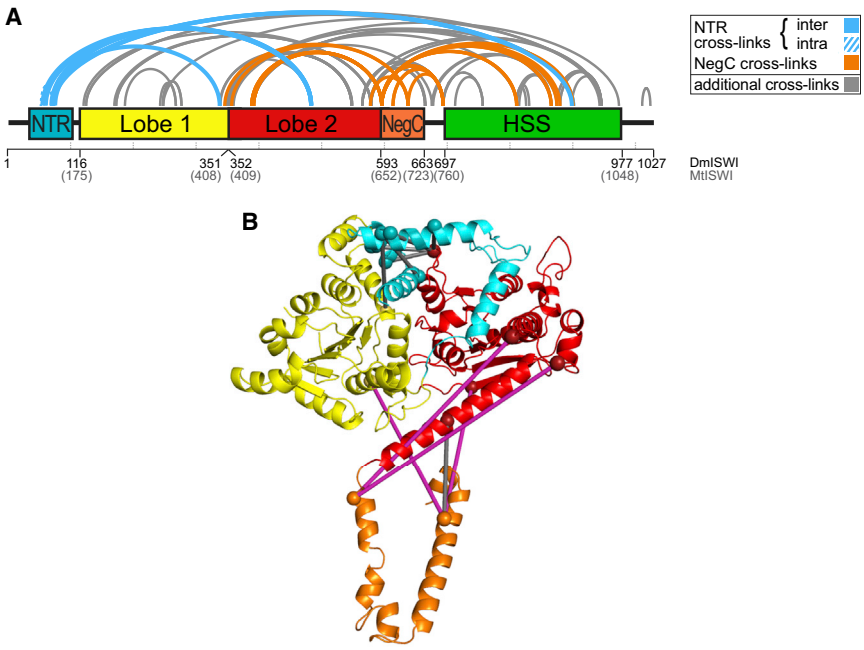

Figure 5. Interaction of the ATPase with the NTR and NegC Domains

(A) Cross-links originating from the NTR and NegC in DmISWI.

(B) NTR and NegC cross-links illustrated in the MtISWI structure (PDB: 5JXR). Most cross-links were compatible with the structure (gray rods). A number of cross-links that connected NegC with the ATPase domain, however, exceeded the maximally allowed distance (purple). See Table S1 for distances spanned by the cross-links. Domains are colored as in (A).

See also Figures S3, S6, and S7 and Table S1.

We queried our cross-linking dataset to differentiate between these competing NegC conformations. Sixteen cross-linked peptides were identified between NegC and the ATPase domain of DmISWI, which came from five unique cross-linking positions (XL 8–12; Table S1). With one exception (XL 8), which connects to the residue at the C-terminus of the model and was discussed above, the cross-links were consistent with the NegC conformation in ScChd1 (Table 1) and with our DmISWI ATPase model (Table S1), which was based on ScChd1. In contrast, most cross-linking distance restraints were violated in the structure of one MtISWI protomer (Figure 5B; Table S1), some severely. In principle, XL 9–12 could be reconciled with the MtISWI structure when considering intermolecular cross-linking of NegC to the neighboring protomer (Table S1; values in brackets). However, size exclusion chromatography of native as well as cross-linked protein did not provide evidence for dimerization (Figure S7), and the monomeric full-length ISWI model showed excellent agreement with the SAXS profile and molecular envelope (Figures 4D and 4E). Attempts to dock the HSS against the ATPase module with a protruding NegC as seen in the MtISWI structure also failed. Sixteen of 18 cross-links (XL 38–55) were violated by the model. In summary, the cross-linking data disfavor the NegC conformation seen in the MtISWI crystal structure. Instead, our data are compatible with a ScChd1-like NegC configuration.

The NTR Contacts the HSS and ATPase Domains

In addition to NegC, the activity of ISWI is regulated by its NTR (Clapier and Cairns, 2012; Ludwigsen et al., 2017; Yan et al., 2016). It has been proposed that the NTR of ISWI may adopt a similar structural architecture as the chromo domains of ScChd1 (Ludwigsen et al., 2017), which connect both ATPase lobes (Hauk et al., 2010). A structural proximity of the NTR to the ATPase lobes was described recently (Ludwigsen et al., 2017; Yan et al., 2016); however, how the NTR is embedded in the overall structure of full-length ISWI remains unclear.

Several cross-links connect the NTR to the rest of the enzyme (XL 13–20 and XL 53–55; Tables S1 and S2, respectively). Most surprising were cross-links between the NTR and the C-terminal end of the HSS domain. These cross-links bridged over 800 amino acids (XL 53–55; Table S2), and indicated spatial proximity, at least temporarily, between the extreme N- and C-terminal domains.

We previously mapped cross-links from the NTR to lobe 2 of the ATPase domain (Ludwigsen et al., 2017). Here, we further identified a connection to lobe 1 (XL 13; Figure 5A and Table S1). All these cross-links from the NTR mapped to residues near the interface formed by the two ATPase lobes in our ISWI model (Figure 4C, blue asterisks), consistent with the NTR stabilizing the ATPase module in the resting conformation. The NTR cross-links were largely satisfied in the MtISWI crystal structure (Figure 5B and Table S1), which suggested that the docking site of the NTR on the ATPase domain is conserved between DmISWI and MtISWI.

DISCUSSION

Structural information for remodeling ATPases has been limited to individual enzyme domains to date, hampering our mechanistic understanding of an important class of enzymes that regulates a wide variety of nuclear processes (Zhou et al., 2016). In this study, we developed an integrative approach to gain insight into the structural architecture of the prototypical chromatin remodeling ATPase ISWI from *Drosophila melanogaster*. Our work showcases how two complementary low-resolution experimental data sources, XL-MS and SAXS, which provide local contacts and global shape information, respectively, can be efficiently integrated into a modeling protocol to reconstruct the structural architecture of proteins. As such, this protocol is complementary to classical structure determination. The value of integrative models has been highlighted by recent efforts of the wwPDB to create a public database (Sali et al., 2015).

Remodeling ATPases are all related to each other, yet their RecA-like ATPase lobes differ drastically in their orientation toward one another in available crystal structures (Durr et al., 2005; Hauk et al., 2010; Thoma et al., 2005; Xia et al., 2016; Yan et al., 2016). We used our integrative modeling approach to reconstruct the conformation of the DmISWI ATPase lobes.

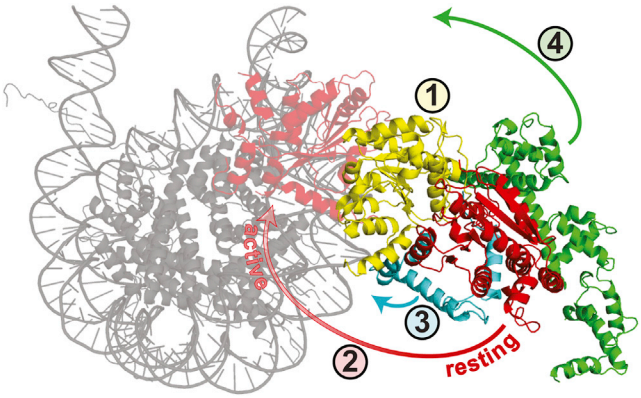

Figure 6. Proposed Structural Changes of DmISWI Upon Nucleosome Binding

In the unbound state, ATPase lobe 1 (yellow) and lobe 2 (dark red) are caged by the NTR (cyan) and the HSS (green) domains. A number of conformational changes are predicted to take place upon docking to the nucleosome to reach the catalytically competent state (arrows; see Discussion for details). Light red: Lobe 2 conformation in the catalytically competent state (Farnung et al., 2017). See also Tables S1 and S2.

After completion of our study, a crystal structure of a thermophilic yeast ISWI protein (MtISWI) became available (Yan et al., 2016). Strikingly, this structure showed ISWI's two ATPase lobes in precisely the same conformation that was predicted by our modeling approach. We conclude that integrative modeling can achieve remarkable accuracy. Moreover, our study provides a strong and independent validation of the unique conformation that MtISWI crystallized in and shows that this conformation is also populated in solution.

We captured the ATPase domain of DmISWI in a repressed configuration with motifs involved in catalysis twisted toward opposite sides. The low basal ATPase activity of $ISWI_{WT}$ and $ISWI_{\Delta HSS}$ (Mueller-Planitz et al., 2013b) likely is a consequence of the repressed state. But how does ISWI become catalytically active? We noted that lobe 1, unlike other nucleosome-interacting interfaces on lobe 2 and on the HSS, could readily dock against the nucleosome without major steric clashes or prior conformational changes (Figure 6, arrow 1). Lobe 2 can then swing over to reach toward its binding site on the nucleosome (arrow 2). This dramatic conformational change is necessary to achieve catalytic competence (Farnung et al., 2017). For lobe 2 to swing over, the NTR and HSS must first detach. These elements would then be available for interactions with other parts of the nucleosome, for instance the acidic patch, which is known to be important for ISWI catalysis (Dann et al., 2017). Release from the ATPase lobes also liberates the DNA-binding interface on the HSS, which now can bind to and measure the length of flanking DNA (arrows 3 and 4) (Dang and Bartholomew, 2007; Leonard and Narlikar, 2015; Yamada et al., 2011).

After measuring the length of flanking DNA, the HSS domain dissociates from flanking DNA and binds closer to the nucleosome core (Leonard and Narlikar, 2015), potentially in a configuration that shares features with the structural state captured by us (Figure 4C). In this state, the HSS domain packs over the ATPase domain, and residues involved in binding flanking DNA are blocked by the ATPase domain, preventing the enzyme from spurious interactions with unrelated DNA. Intimate contacts between the HSS and ATPase domain in this state may allow the HSS domain to allosterically regulate the ATPase domain and sense and respond to motions of the ATPase lobes during the ATP hydrolysis cycle.

A previous study mutated residues in the predicted ATPase-HSS interface of ScISW2 (Figure S6D; Hota et al., 2013). Unexpectedly, DNA and nucleosome affinities were not appreciably affected by the mutations, whereas ATP turnover and nucleosome sliding were strongly reduced. These results suggest that the HSS-ATPase interface may be functionally important for catalysis and invite further investigation.

The reconstruction of the architecture of full-length ISWI provided unexpected structural insight into the enzyme's autoregulation. Cross-links between the NTR and the SLIDE domain indicated spatial proximity of the extreme N- and C-terminal domains of ISWI. Both domains thereby cage the catalytic core of the enzyme. Consistent with structural proximity of the termini, it is possible to observe fluorescence resonance energy transfer between fluorescent proteins that are fused to the N- and C-terminus of the human ISWI homolog Snf2H (F. Erdel and K. Rippe, personal communication). Moreover, a similar structural arrangement was seen recently for ScChd1 (Farnung et al., 2017; Sundaramoorthy et al., 2017), suggesting a shared structural architecture among remodeling enzymes. This configuration is expected to break up to allow the HSS domain to reach its binding site on the DNA that flanks the nucleosome (Figure 6).

Two conformations of the NegC domain have been detected in the crystal structures of MtISWI and ScChd1 (Hauk et al., 2010; Yan et al., 2016). Whereas the NegC domain in ScChd1 packs against the surface of both ATPase lobes within one protomer, NegC of MtISWI protrudes from the globular protein and interacts with a neighboring MtISWI molecule in the crystal. Consistent with ISWI being predominantly monomeric in solution (Forné et al., 2012; Mueller-Planitz et al., 2013b; Racki et al., 2009; Yan et al., 2016), our cross-linking data support a NegC conformation as seen in ScChd1 but not MtISWI. Of note, the NegC domain of one MtISWI protomer in the crystal packs against the ATPase domain of the second protomer in a conformation that was strikingly similar to ScChd1 (Figure S3D). Thus, we propose that the MtISWI-like NegC conformation can be promoted by induced proximity, for example, in the crystal or when two ISWI molecules are bound to the same nucleosome. Future work will be necessary to assess the functional relevance of this and the several other predicted conformational changes.

STAR★METHODS

Detailed methods are provided in the online version of this paper and include the following:

- KEY RESOURCES TABLE
- CONTACT FOR REAGENT AND RESOURCE SHARING
- EXPERIMENTAL MODEL AND SUBJECT DETAILS
  - Bacterial Strains Used for Protein Expression
- METHOD DETAILS
  - Protein Expression and Purification
  - ATPase Assay
  - UV Cross-Linking Reaction

SUPPLEMENTAL INFORMATION

Supplemental Information includes seven figures and two tables and can be found with this article online at https://doi.org/10.1016/j.str.2017.12.015.

ACKNOWLEDGMENTS

We thank Peter Becker (LMU Munich, Germany) and Sebastian Doniach (Stanford University) for discussions and support in the initial stages of this project, Gianluca Santoni and Sönke Seifert for help with measurements at beamlines BM29 at the ESRF (Grenoble) and 12ID at the APS (Argonne, IL), and members of the Müller-Planitz laboratory and the ZfP (LMU Munich, Germany) for discussions. N.H. is thankful for support by the Integrated Research Training Group (IRTG 1064) graduate program. J. Ludwigsen is grateful to the Schering Stiftung for a predoctoral fellowship. C.E.M.S. and F.M.-P. acknowledge funding by the Center for Integrated Protein Science Munich. This work was supported by DFG grants MU 3613/1-1 and MU 3613/3-1, SFB 1064/1 TP-A07 and SFB 863.

AUTHOR CONTRIBUTIONS

Conceptualization, F.M.-P., J. Lipfert; Methodology, N.H., C.E.M.S., I.F., A.I., J. Lipfert, M.Z., and F.M.-P.; Software, C.E.M.S. and F.M.-P.; Investigation, N.H., C.E.M.S., L.K.B., I.F., J. Lipfert, J. Ludwigsen, and F.M.-P.; Writing – Original Draft, N.H. and F.M.-P.; Writing – Review & Editing, N.H., C.E.M.S., L.B., I.F., J. Lipfert, and F.M.-P.; Visualization, N.H., C.E.M.S., and L.K.B.; Supervision, M.Z., J. Lipfert, and F.M.-P.; Funding Acquisition, M.Z., J. Lipfert, A.I., and F.M.-P.

DECLARATION OF INTERESTS

None.

Received: April 24, 2017
Revised: October 25, 2017
Accepted: December 27, 2017
Published: January 25, 2018

REFERENCES

Berman, H.M., Westbrook, J., Feng, Z., Gilliland, G., Bhat, T.N., Weissig, H., Shindyalov, I.N., and Bourne, P.E. (2000). The protein data bank. Nucleic Acids Res. *28*, 235–242.

Clapier, C.R., and Cairns, B.R. (2012). Regulation of ISWI involves inhibitory modules antagonized by nucleosomal epitopes. Nature *492*, 280–284.

Dang, W., and Bartholomew, B. (2007). Domain architecture of the catalytic subunit in the ISW2-nucleosome complex. Mol. Cell. Biol. *27*, 8306–8317.

Dann, G.P., Liszczak, G.P., Bagert, J.D., Muller, M.M., Nguyen, U.T.T., Wojcik, F., Brown, Z.Z., Bos, J., Panchenko, T., Pihl, R., et al. (2017). ISWI chromatin remodellers sense nucleosome modifications to determine substrate preference. Nature *548*, 607–611.

de Vries, S.J., Schindler, C.E., Chauvot de Beauchene, I., and Zacharias, M. (2015). A web interface for easy flexible protein-protein docking with ATTRACT. Biophys. J. *108*, 462–465.

Dolinsky, T.J., Czodrowski, P., Li, H., Nielsen, J.E., Jensen, J.H., Klebe, G., and Baker, N.A. (2007). PDB2PQR: expanding and upgrading automated preparation of biomolecular structures for molecular simulations. Nucleic Acids Res. *35*, W522–W525.

Dolinsky, T.J., Nielsen, J.E., McCammon, J.A., and Baker, N.A. (2004). PDB2PQR: an automated pipeline for the setup of Poisson-Boltzmann electrostatics calculations. Nucleic Acids Res. *32*, W665–W667.

Durr, H., Flaus, A., Owen-Hughes, T., and Hopfner, K.P. (2006). Snf2 family ATPases and DExx box helicases: differences and unifying concepts from high-resolution crystal structures. Nucleic Acids Res. *34*, 4160–4167.

Durr, H., Korner, C., Muller, M., Hickmann, V., and Hopfner, K.P. (2005). X-ray structures of the *Sulfolobus solfataricus* SWI2/SNF2 ATPase core and its complex with DNA. Cell *121*, 363–373.

Emekli, U., Schneidman-Duhovny, D., Wolfson, H.J., Nussinov, R., and Haliloglu, T. (2008). HingeProt: automated prediction of hinges in protein structures. Proteins *70*, 1219–1227.

Farnung, L., Vos, S.M., Wigge, C., and Cramer, P. (2017). Nucleosome-Chd1 structure and implications for chromatin remodelling. Nature *550*, 539–542.

Fiorucci, S., and Zacharias, M. (2010). Binding site prediction and improved scoring during flexible protein-protein docking with ATTRACT. Proteins *78*, 3131–3139.

Fischer, L., Chen, Z.A., and Rappsilber, J. (2013). Quantitative cross-linking/mass spectrometry using isotope-labelled cross-linkers. J. Proteomics *88*, 120–128.

Flaus, A., Martin, D.M., Barton, G.J., and Owen-Hughes, T. (2006). Identification of multiple distinct Snf2 subfamilies with conserved structural motifs. Nucleic Acids Res. *34*, 2887–2905.

Forné, I., Ludwigsen, J., Imhof, A., Becker, P.B., and Mueller-Planitz, F. (2012). Probing the conformation of the ISWI ATPase domain with genetically encoded photoreactive crosslinkers and mass spectrometry. Mol. Cell Proteomics *11*, M111.012088.

Franke, D., and Svergun, D.I. (2009). DAMMIF, a program for rapid ab-initio shape determination in small-angle scattering. J. Appl. Crystallogr. *42*, 342–346.

Garraway, L.A., and Lander, E.S. (2013). Lessons from the cancer genome. Cell *153*, 17–37.

Grune, T., Brzeski, J., Eberharter, A., Clapier, C.R., Corona, D.F., Becker, P.B., and Muller, C.W. (2003). Crystal structure and functional analysis of a nucleosome recognition module of the remodeling factor ISWI. Mol. Cell *12*, 449–460.

Guinier, A. (1939). La diffraction des rayons X aux tres petits angles: applications a l'etude de phenomenes ultramicroscopiques. Ann. Phys. *12*, 161–237.

Hauk, G., McKnight, J.N., Nodelman, I.M., and Bowman, G.D. (2010). The chromodomains of the Chd1 chromatin remodeler regulate DNA access to the ATPase motor. Mol. Cell *39*, 711–723.

Herzog, F., Kahraman, A., Boehringer, D., Mak, R., Bracher, A., Walzthoeni, T., Leitner, A., Beck, M., Hartl, F.U., Ban, N., et al. (2012). Structural probing of a protein phosphatase 2A network by chemical cross-linking and mass spectrometry. Science *337*, 1348–1352.

Holding, A.N. (2015). XL-MS: protein cross-linking coupled with mass spectrometry. Methods *89*, 54–63.

Hota, S.K., Bhardwaj, S.K., Deindl, S., Lin, Y.C., Zhuang, X., and Bartholomew, B. (2013). Nucleosome mobilization by ISW2 requires the concerted action of the ATPase and SLIDE domains. Nat. Struct. Mol. Biol. *20*, 222–229.

Humphrey, W., Dalke, A., and Schulten, K. (1996). VMD: visual molecular dynamics. J. Mol. Graph. *14*, 33–38, 27-8.

Jorgensen, W.L., and Tirado-Rives, J. (1988). The OPLS [optimized potentials for liquid simulations] potential functions for proteins, energy minimizations for crystals of cyclic peptides and crambin. J. Am. Chem. Soc. *110*, 1657–1666.

Kadoch, C., and Crabtree, G.R. (2015). Mammalian SWI/SNF chromatin remodeling complexes and cancer: mechanistic insights gained from human genomics. Sci. Adv. *1*, e1500447.

Koch, M.H., Vachette, P., and Svergun, D.I. (2003). Small-angle scattering: a view on the properties, structures and structural changes of biological macromolecules in solution. Q. Rev. Biophys. *36*, 147–227.

Konarev, P.V., Volkov, V.V., Sokolova, A.V., Koch, M.H., and Svergun, D.I. (2003). PRIMUS: a Windows PC-based system for small-angle scattering data analysis. J. Appl. Crystallogr. *36*, 1277–1282.

Kozin, M.B., and Svergun, D.I. (2001). Automated matching of high-and low-resolution structural models. J. Appl. Crystallogr. *34*, 33–41.

Leitner, A., Reischl, R., Walzthoeni, T., Herzog, F., Bohn, S., Forster, F., and Aebersold, R. (2012). Expanding the chemical cross-linking toolbox by the use of multiple proteases and enrichment by size exclusion chromatography. Mol. Cell Proteomics *11*, M111.014126.

Leonard, J.D., and Narlikar, G.J. (2015). A nucleotide-driven switch regulates flanking DNA length sensing by a dimeric chromatin remodeler. Mol. Cell *57*, 850–859.

Lewis, R., Durr, H., Hopfner, K.P., and Michaelis, J. (2008). Conformational changes of a Swi2/Snf2 ATPase during its mechano-chemical cycle. Nucleic Acids Res. *36*, 1881–1890.

Li, H., Robertson, A.D., and Jensen, J.H. (2005). Very fast empirical prediction and rationalization of protein pKa values. Proteins *61*, 704–721.

Lieleg, C., Ketterer, P., Nuebler, J., Ludwigsen, J., Gerland, U., Dietz, H., Mueller-Planitz, F., and Korber, P. (2015). Nucleosome spacing generated by ISWI and CHD1 remodelers is constant regardless of nucleosome density. Mol. Cell. Biol. *35*, 1588–1605.

Linge, J.P., and Nilges, M. (1999). Influence of non-bonded parameters on the quality of NMR structures: a new force field for NMR structure calculation. J. Biomol. NMR *13*, 51–59.

Lipfert, J., and Doniach, S. (2007). Small-angle X-ray scattering from RNA, proteins, and protein complexes. Annu. Rev. Biophys. Biomol. Struct. *36*, 307–327.

Lossl, P., Kolbel, K., Tanzler, D., Nannemann, D., Ihling, C.H., Keller, M.V., Schneider, M., Zaucke, F., Meiler, J., and Sinz, A. (2014). Analysis of nidogen-1/laminin gamma1 interaction by cross-linking, mass spectrometry, and computational modeling reveals multiple binding modes. PLoS One *9*, e112886.

Ludwigsen, J., Pfennig, S., Singh, A.K., Schindler, C., Harrer, N., Forne, I., Zacharias, M., and Mueller-Planitz, F. (2017). Concerted regulation of ISWI by an autoinhibitory domain and the H4 N-terminal tail. Elife *6*, e21477.

Luger, K., Mader, A.W., Richmond, R.K., Sargent, D.F., and Richmond, T.J. (1997). Crystal structure of the nucleosome core particle at 2.8 A resolution. Nature *389*, 251–260.

McKnight, J.N., Jenkins, K.R., Nodelman, I.M., Escobar, T., and Bowman, G.D. (2011). Extranucleosomal DNA binding directs nucleosome sliding by Chd1. Mol. Cell. Biol. *31*, 4746–4759.

Merkley, E.D., Rysavy, S., Kahraman, A., Hafen, R.P., Daggett, V., and Adkins, J.N. (2014). Distance restraints from crosslinking mass spectrometry: mining a molecular dynamics simulation database to evaluate lysine-lysine distances. Protein Sci. *23*, 747–759.

Mueller-Planitz, F. (2015). Crossfinder-assisted mapping of protein crosslinks formed by site-specifically incorporated crosslinkers. Bioinformatics *31*, 2043–2045.

Mueller-Planitz, F., Klinker, H., and Becker, P.B. (2013a). Nucleosome sliding mechanisms: new twists in a looped history. Nat. Struct. Mol. Biol. *20*, 1026–1032.

Mueller-Planitz, F., Klinker, H., Ludwigsen, J., and Becker, P.B. (2013b). The ATPase domain of ISWI is an autonomous nucleosome remodeling machine. Nat. Struct. Mol. Biol. *20*, 82–89.

Narlikar, G.J., Sundaramoorthy, R., and Owen-Hughes, T. (2013). Mechanisms and functions of ATP-dependent chromatin-remodeling enzymes. Cell *154*, 490–503.

Pernot, P., Round, A., Barrett, R., De Maria Antolinos, A., Gobbo, A., Gordon, E., Huet, J., Kieffer, J., Lentini, M., Mattenet, M., et al. (2013). Upgraded ESRF BM29 beamline for SAXS on macromolecules in solution. J. Synchrotron Radiat. *20*, 660–664.

Petoukhov, M.V., Franke, D., Shkumatov, A.V., Tria, G., Kikhney, A.G., Gajda, M., Gorba, C., Mertens, H.D., Konarev, P.V., and Svergun, D.I. (2012). New developments in the ATSAS program package for small-angle scattering data analysis. J. Appl. Crystallogr. *45*, 342–350.

Petoukhov, M.V., and Svergun, D.I. (2005). Global rigid body modeling of macromolecular complexes against small-angle scattering data. Biophys. J. *89*, 1237–1250.

Putnam, C.D., Hammel, M., Hura, G.L., and Tainer, J.A. (2007). X-ray solution scattering (SAXS) combined with crystallography and computation: defining accurate macromolecular structures, conformations and assemblies in solution. Q. Rev. Biophys. *40*, 191–285.

Racki, L.R., Yang, J.G., Naber, N., Partensky, P.D., Acevedo, A., Purcell, T.J., Cooke, R., Cheng, Y., and Narlikar, G.J. (2009). The chromatin remodeller ACF acts as a dimeric motor to space nucleosomes. Nature *462*, 1016–1021.

Racki, L.R., Naber, N., Pate, E., Leonard, J.D., Cooke, R., and Narlikar, G.J. (2014). The histone H4 tail regulates the conformation of the ATP-binding pocket in the SNF2h chromatin remodeling enzyme. J. Mol. Biol. *426*, 2034–2044.

Saha, A., Wittmeyer, J., and Cairns, B.R. (2005). Chromatin remodeling through directional DNA translocation from an internal nucleosomal site. Nat. Struct. Mol. Biol. *12*, 747–755.

Sali, A., Berman, H.M., Schwede, T., Trewhella, J., Kleywegt, G., Burley, S.K., Markley, J., Nakamura, H., Adams, P., Bonvin, A.M., et al. (2015). Outcome of the first wwPDB Hybrid/Integrative methods task force workshop. Structure *23*, 1156–1167.

Schindler, C.E., de Vries, S.J., and Zacharias, M. (2015). iATTRACT: simultaneous global and local interface optimization for protein-protein docking refinement. Proteins *83*, 248–258.

Schneidman-Duhovny, D., Hammel, M., Tainer, J.A., and Sali, A. (2013). Accurate SAXS profile computation and its assessment by contrast variation experiments. Biophys. J. *105*, 962–974.

Schneidman-Duhovny, D., Pellarin, R., and Sali, A. (2014). Uncertainty in integrative structural modeling. Curr. Opin. Struct. Biol. *28*, 96–104.

Schwanbeck, R., Xiao, H., and Wu, C. (2004). Spatial contacts and nucleosome step movements induced by the NURF chromatin remodeling complex. J. Biol. Chem. *279*, 39933–39941.

Singleton, M.R., Dillingham, M.S., and Wigley, D.B. (2007). Structure and mechanism of helicases and nucleic acid translocases. Annu. Rev. Biochem. *76*, 23–50.

Sundaramoorthy, R., Hughes, A.L., Singh, V., Wiechens, N., Ryan, D.P., El-Mkami, H., Petoukhov, M., Svergun, D.I., Treutlein, B., Quack, S., et al. (2017). Structural reorganization of the chromatin remodeling enzyme Chd1 upon engagement with nucleosomes. Elife *6*, e22510.

Svergun, D.I., Barberato, C., and Koch, M.H.J. (1995). CRYSOL - a program to evaluate X-ray solution scattering of biological macromolecules from atomic coordinates. J. Appl. Cryst. *28*, 768–773.

Swygert, S.G., and Peterson, C.L. (2014). Chromatin dynamics: interplay between remodeling enzymes and histone modifications. Biochim. Biophys. Acta *1839*, 728–736.

Taylor, A.F., Amundsen, S.K., Guttman, M., Lee, K.K., Luo, J., Ranish, J., and Smith, G.R. (2014). Control of RecBCD enzyme activity by DNA binding- and Chi hotspot-dependent conformational changes. J Mol. Biol. *426*, 3479–3499.

Thoma, N.H., Czyzewski, B.K., Alexeev, A.A., Mazin, A.V., Kowalczykowski, S.C., and Pavletich, N.P. (2005). Structure of the SWI2/SNF2 chromatin-remodeling domain of eukaryotic Rad54. Nat. Struct. Mol. Biol. *12*, 350–356.

Volkov, V.V., and Svergun, D.I. (2003). Uniqueness of ab initio shape determination in small-angle scattering. J. Appl. Crystallogr. *36*, 860–864.

Walzthoeni, T., Claassen, M., Leitner, A., Herzog, F., Bohn, S., Forster, F., Beck, M., and Aebersold, R. (2012). False discovery rate estimation for cross-linked peptides identified by mass spectrometry. Nat. Methods *9*, 901–903.

Webb, B., and Sali, A. (2016). Comparative protein structure modeling using MODELLER. Curr. Protoc. Protein Sci. *86*, 2.9.1–2.9.37.

Wittelsberger, A., Thomas, B.E., Mierke, D.F., and Rosenblatt, M. (2006). Methionine acts as a "magnet" in photoaffinity crosslinking experiments. FEBS Lett. *580*, 1872–1876.

Wriggers, W., Milligan, R.A., and McCammon, J.A. (1999). Situs: a package for docking crystal structures into low-resolution maps from electron microscopy. J. Struct. Biol. *125*, 185–195.

Xia, X., Liu, X., Li, T., Fang, X., and Chen, Z. (2016). Structure of chromatin remodeler Swi2/Snf2 in the resting state. Nat. Struct. Mol. Biol. *23*, 722–729.

Yamada, K., Frouws, T.D., Angst, B., Fitzgerald, D.J., DeLuca, C., Schimmele, K., Sargent, D.F., and Richmond, T.J. (2011). Structure and mechanism of the chromatin remodelling factor ISW1a. Nature *472*, 448–453.

Yan, L., Wang, L., Tian, Y., Xia, X., and Chen, Z. (2016). Structure and regulation of the chromatin remodeller ISWI. Nature *540*, 466–469.

Yang, J.G., Madrid, T.S., Sevastopoulos, E., and Narlikar, G.J. (2006). The chromatin-remodeling enzyme ACF is an ATP-dependent DNA length sensor that regulates nucleosome spacing. Nat. Struct. Mol. Biol. *13*, 1078–1083.

Zacharias, M. (2003). Protein-protein docking with a reduced protein model accounting for side-chain flexibility. Protein Sci. *12*, 1271–1282.

Zhou, C.Y., Johnson, S.L., Gamarra, N.I., and Narlikar, G.J. (2016). Mechanisms of ATP-dependent chromatin remodeling motors. Annu. Rev. Biophys. *45*, 153–181.

Zofall, M., Persinger, J., Kassabov, S.R., and Bartholomew, B. (2006). Chromatin remodeling by ISW2 and SWI/SNF requires DNA translocation inside the nucleosome. Nat. Struct. Mol. Biol. *13*, 339–346.

STAR★METHODS

KEY RESOURCES TABLE

REAGENT or RESOURCE	SOURCE	IDENTIFIER
Bacterial and Virus Strains		
E.coli BL21-Gold(DE3)	Agilent Technologies	Cat#230132
Chemicals, Peptides, and Recombinant Proteins		
Adenosine triphosphate (ATP)	Sigma	Cat#A3377
Ammonium bicarbonate (NH_4HCO_3)	Sigma	Cat#09830
BS^2G–H4/D4	ProteoChem	Cat#c1126/h5101
BS^3–H4	ProteoChem	Cat#c1103
DMSO	Life technologies	Cat#D12345
Lactate dehydrogenase/pyruvate kinase (LDH/PK)	Sigma	Cat#P0294
Nicotinamidadenindinucleotide (NADH)	Sigma	Cat#N1636
Phosphoenolpyruvate (PEP)	Molekula	Cat#16921512
Salmon Sperm DNA Solution	ThermoFisher Scientific	Cat#15632011
TEV protease	In-house preparation	N/A
Trypsin	Promega	Cat#V511B
Oligonucleotides		
Mutagenesis primer ISWI K337D #1: GTGCTGGA CCCTTTCCTGCTCCGTCGTC	This study	N/A
Mutagenesis primer ISWI K337D #2: CAGGAAAG GGTCCAGCACGGCATGCAAAC	This study	N/A
Mutagenesis primer ISWI D485K #1: CACGAAAA GCGTAACAGGCAGATTCAGGAA	This study	N/A
Mutagenesis primer ISWI D485K #2: CCTGTTAC GCTTTTCGTGCGGCGTCTGA	This study	N/A
Recombinant DNA		
pPROEX-HTb plasmid encoding $DmISWI_{1–1027}$; pFMP210	(Forné et al., 2012)	N/A
pPROEX-HTb plasmid encoding $DmISWI_{26–648}$; pFMP114	Gift from C. Müller; EMBL, Heidelberg, Germany	N/A
pPROEX-HTb plasmid encoding $DmISWI_{M578B}$; pFMP163	(Forné et al., 2012)	N/A
pPROEX-HTb plasmid encoding $DmISWI_{K337D}$; pFMP383	This study	N/A
pPROEX-HTb plasmid encoding $DmISWI_{D485K}$; pFMP384	This study	N/A
pPROEX-HTb plasmid encoding $DmISWI_{K337D\ D485K}$; pFMP386	This study	N/A
Software and Algorithms		
ATTRACT	This study and (de Vries et al., 2015; Schindler et al., 2015)	www.attract.ph.tum.de
Bio-Rad Image Lab 5.2.1	Bio-Rad	http://www.bio-rad.com/
BUNCH	(Petoukhov and Svergun, 2005)	https://www.embl-hamburg.de/biosaxs/bunch.html
Crossfinder	This study and (Mueller-Planitz, 2015)	http://www.molekularbiologie.abi.med.uni-muenchen.de/ueber_uns/mueller_planitz/publications/index.html
CRYSOL	(Petoukhov et al., 2012)	https://www.embl-hamburg.de/biosaxs/crysol.html

(*Continued on next page*)

Continued

REAGENT or RESOURCE	SOURCE	IDENTIFIER
DAMAVER	(Volkov and Svergun, 2003)	https://www.embl-hamburg.de/biosaxs/software.html
DAMMIF	(Franke and Svergun, 2009)	https://www.embl-hamburg.de/biosaxs/software.html
FOXS	(Schneidman-Duhovny et al., 2013)	https://modbase.compbio.ucsf.edu/foxs/
KaleidaGraph 4.03 software	Synergy Software	www.synergy.com
Matlab 2015	The MathWorks Inc., Natick, MA, USA	https://de.mathworks.com/
MODELLER	(Webb and Sali, 2016).	https://salilab.org/modeller/
PDB2PQR	(Dolinsky et al., 2004)	http://nbcr-222.ucsd.edu/pdb2pqr_2.0.0/
PRIMUS	(Konarev et al., 2003)	https://www.embl-hamburg.de/biosaxs/software.html
PropKa	(Li et al., 2005)	propka.org/
Proteome Discoverer 1.4, PostSearch Recalibrator Node	ThermoFisher Scientific	https://www.thermofisher.com
Proteowizard, msconvert	Proteowizard	proteowizard.sourceforge.net/tools.shtml
PyMOL, version 1.30	PyMOL	https://www.pymol.org/
SITUS package, version 2.7.2	(Wriggers et al., 1999)	http://situs.biomachina.org
Visual molecular dynamics (VMD)	(Humphrey et al., 1996)	http://www.ks.uiuc.edu/Research/vmd/
Xcalibur	ThermoFisher Scientific	https://www.thermofisher.com
HingeProt	(Emekli et al., 2008)	http://bioinfo3d.cs.tau.ac.il/HingeProt/
Other		
15-cm analytical column C18 nanocolumn (75μm ID homepacked with ReproSil-Pur C18-AQ 2.4 μm)	N/A	N/A
384 well plates	Greiner	Cat#781101
Bio-Link 365 UV-Crosslinker	Viber	Cat#60-BLX-365
C18 ZipTips	Agilent Technologies	Cat#A57003100
Centrifuge filter with 0.22 μm pore size	Merck Millipore	Cat#UFC30GV25
HiLoad 16/600 Superdex 200	GE Healthcare	Cat#28-9893-35
HisTrap HP, 1 ml	GE Healthcare	Cat#17-5247-01
HisTrap HP, 5 ml	GE Healthcare	Cat#17-5248-02
LM10 Microfluidizer	Microfluidics	https://www.microfluidicscorp.com/microfluidizers/lab-machines/lm10/
LTQ-Orbitrap XL mass spectrometer	ThermoFisher Scientific	www.thermofisher.com/order/catalog/product/IQLAAEGAAPFADBMAOK
Mono Q 5/50 GL	GE Healthcare	Cat#17-5166-01
Mono S 5/50 GL	GE Healthcare	Cat#17-5168-01
PowerWave HT 384 well plate reader	BioTek	https://www.biotek.com/products/detection-microplate-readers/powerwave-ht-microplate-spectrophotometer/
Q Exactive HF mass spectrometer	ThermoFisher Scientific	www.thermofisher.com/order/catalog/product/IQLAAEGAAPFALvGMBFZ
ReproSil-Pur C18-AQ 2.4 μm	Dr. Maisch GmbH	Cat#r124.aq.0001
Sep-Pak tC18 Cartridges	Waters	Cat#WAT043410
Superdex 200 10/300 GL	GE Healthcare	Cat#17-5175-01
Superdex 200 Increase 10/300 GL	GE Healthcare	Cat#28990944
Superdex Peptide PC 3.2/300	GE Healthcare	Cat#29036231
Ultimate 3000 HPLC system	ThermoFisher Scientific	www.thermofisher.com/order/catalog/product/IQLAAAGABHFAPBMBFD
Ultimate 3000 RSLCnano system	ThermoFisher Scientific	www.thermofisher.com/order/catalog/product/ULTIM3000RSLCNANO

CONTACT FOR REAGENT AND RESOURCE SHARING

Further information and requests for resources and reagents should be directed to and will be fulfilled by the Lead Contact, Felix Mueller-Planitz (fmueller@bmc.med.lmu.de).

EXPERIMENTAL MODEL AND SUBJECT DETAILS

Bacterial Strains Used for Protein Expression

For expression of all ISWI variants of this study, we used pPROEX-HTb–based expression plasmids with genes encoding wild type, full-length Drosophila $ISWI_{1–1027}$, referred to as $ISWI_{WT}$, $ISWI_{26–648}$ ($ISWI_{\Delta HSS}$) or $ISWI_{M578B}$, respectively. Point mutations ($ISWIK_{337D}$, $ISWI_{D485K}$ and $ISWI_{K337D\ D485K}$) were introduced into $ISWI_{WT}$ by Gibson cloning and the constructs were fully sequence verified before transformation.

METHOD DETAILS

Protein Expression and Purification

The recombinant proteins were expressed with an N-terminally fused His_6-TEV tag in *E. coli* BL21-Gold(DE3). The cells were cultured in LB-ampicillin media at 37°C to OD_{600} of 0.6-0.8 before transferring to 18°C for an induction overnight with 0.2 mM IPTG. Harvested and resuspended cells were lysed by French press and sonication or by LM10 Microfluidizer. Purification of ISWI proteins were performed essentially as described (Forné et al., 2012; Ludwigsen et al., 2017). All enzyme variants were initially affinity purified using a nickel resin (HisTrap HP, 1 or 5 ml; GE Healthcare). The His_6-TEV tag was cleaved off by TEV protease (1:80 (w/w); prepared in-house) overnight at 4°C for all enzymes except $ISWI_{\Delta HSS}$. The cleaved tag and the protease were removed by passing the protein solution a second time through the Ni^{2+}-affinity chromatography column. Proteins were further purified by ion exchange ($ISWI_{\Delta HSS}$: Mono Q 5/50 GL ion exchange column; $ISWI_{WT}$ and $ISWI_{M578B}$: Mono S 5/50 GL ion exchange column; GE Healthcare) and size exclusion chromatography (SEC; Superdex 200 10/300 GL or Increase 10/300 GL or HiLoad 16/60 Superdex 200; GE Healthcare).

ATPase Assay

The ATP-hydrolysis was essentially measured as described (Forné et al., 2012) in a coupled assay using pyruvate kinase (15.5 U/mL), phosphoenolpyruvate (6 mM), lactate dehydrogenase (15.5 U/mL) and NADH (1.2 mM). Each 30 μL reaction was carried out in 25 mM Hepes-KOH pH 7.6, 3 mM $MgCl_2$, 0.1 mM EDTA, 10% glycerol, 50 mM NaCl, 0.2 mg/ml BSA at 26°C in 384 well plates (Greiner). Enzyme (300 nM) was pre-incubated with varying amounts (0 to 1.3 g/l) of salmon sperm DNA (ThermoFischer). The reactions were initiated by the addition of saturating ATP-Mg^{2+} (3 mM). The absorption of NADH was read by a Biotek PowerWave HT 384 well plate reader over 30 min. From linear fits to the data, ATPase activities were calculated. The ATPase activities for the varying DNA concentrations were fitted to the Michaelis-Menten equation using KaleidaGraph 4.03 software to determine the maximal catalytic rate (k_{cat}) values at saturating DNA concentrations. To ensure comparability of the enzyme amounts, a portion of the reaction mixtures was analyzed by SDS-Page stained with Coomassie Blue, and bands corresponding to ISWI were quantified with Bio-Rad Image Lab 5.2.1 software (Figure S4B).

UV Cross-Linking Reaction

We mined two previously published datasets for Bpa-induced cross-links, one for $ISWI_{H483B}$ (Ludwigsen et al., 2017) and one for $ISWI_{M578B}$ (Forné et al., 2012). Furthermore, we collected an additional dataset for $ISWI_{M578B}$. Cross-linking was performed in 25 mM Hepes-KOH pH 7.6, 0.1 mM EDTA, 10% glycerol, 100 mM KOAc, 1.5 mM $MgCl_2$, 1 mM DTT on ice in a Bio-Link UV-Cross-linker (Vilber) at 365 nm for up to 2 hours. UV-irradiated samples and an unirradiated control sample were separated by SDS-PAGE and subsequently Coomassie stained. Protein bands were excised and in-gel trypsin digested. Extracted peptides were purified using C18 ZipTips (Agilent Technologies) and re-suspended in 0.1% trifluoroacetic acid (TFA) before LC-MS/MS analysis was performed.

Chemical Cross-Linking Reactions

Cross-linking reactions contained 1.0 to 1.5 μM purified protein in 25 mM Hepes-KOH pH 7.6, 0.1 mM EDTA, 10% glycerol, 100 mM KOAc, 1.5 mM $MgCl_2$, 2 mM DTT. The cross-linkers BS^2G or BS^3 (ProteoChem) were freshly dissolved in DMSO and added to a final concentration of 0.5 to 3 mM. The cross-linking reactions and a DMSO-treated control were incubated on ice or at 30°C and quenched after 30 min by adding NH_4HCO_3 to a final concentration of 200 mM for 20 min. Samples were precipitated by the addition of 15% (w/v) trichloroacetic acid (TCA), and the pellet was washed twice with acetone. Selected samples were size separated by SEC (Superdex 200 10/300 GL or Superdex 200 Increase 10/300 GL, GE Healthcare; 50 mM Hepes-KOH pH 7.6, 0.2 mM EDTA, 200 mM KOAc, 1 mM DTT; see column 'Size selection' in Tables S1 and S2). All samples were subsequently precipitated by the addition of 15% (w/v) trichloroacetic acid (TCA), and the pellet was washed twice with acetone.

The TCA pellets were solubilized in urea solution (6 M urea, 2 M thiourea, 10 mM Hepes-KOH pH 8.0, 200 mM NH_4HCO_3), reduced with 50 mM DTT for 1 h at room temperature, alkylated with 100 mM iodoacetamide for 30 min in the dark and digested with trypsin (enzyme to substrate ratio 1:50) overnight at 37°C. The peptide samples were further purified and concentrated by a C18 resin (C18

ZipTips, Agilent Technologies or Sep-Pak tC18 Cartridges, Waters). To enrich cross-linked peptides over un-modified peptides, size exclusion chromatography was performed for selected samples. A Superdex Peptide PC 3.2/300 (GE Healthcare) was pre-equilibrated with 30% (v/v) acetonitrile 0.1% (v/v) TFA as mobile phase. Fractions were collected every 2 min at a flow rate of 50 μl/min. Prior to LC-MS/MS analysis fractions were resuspended in 0.1% TFA.

Mapping of Cross-Links by LC-MS/MS

Samples were injected in an Ultimate 3000 (Thermo) or RSLCnano system (Thermo) and separated in a 15-cm analytical column C18 nanocolumn (75 μm ID homepacked with ReproSil-Pur C18-AQ 2.4 μm, Dr. Maisch) with a 40 or 60 min gradient from 5 to 60% acetonitrile in 0.1% formic acid. The effluent from the HPLC was directly electrosprayed into an LTQ-Orbitrap XL or into a Q Exactive HF (Thermo). In both cases, all precursors and corresponding fragment ions were measured with high resolution and high accuracy. The instruments were operated in the data-dependent mode to automatically switch between full scan MS and MS/MS acquisition. For the LTQ-Orbitrap XL measurements, survey full scan MS spectra (from m/z 300–2000) were acquired with resolution R = 60,000 at m/z 400. The six most intense peptide ions with charge states between 2 and 5 were sequentially isolated to a target value of 10,000 and fragmented in the linear ion trap by collision induced dissociation (CID). Product ion spectra were recorded in the Orbitrap part of the instrument. For all measurements with the Orbitrap detector, 3 lock mass ions from ambient air (m/z = 371.10123, 445.12002, 519.13882) were used for internal calibration as described in (Forné et al., 2012). Typical mass spectrometric conditions were: spray voltage, 1.4 kV; no sheath and auxiliary gas flow; heated capillary temperature, 200°C; normalized collision energy, 35% for CID in LTQ. The ion selection threshold was 10,000 counts for MS2. An activation q = 0.25 and activation time of 30 ms were used. For the Q Exactive HF measurements, survey full scan MS spectra (from m/z 375–1600) were acquired with resolution as above (AGC target of $3x10^6$). The ten most intense peptide ions with charge states between 3 and 5 were sequentially isolated to a target value of $1x10^5$, and fragmented at 27% normalized collision energy. Typical mass spectrometric conditions were: spray voltage, 1.5 kV; no sheath and auxiliary gas flow; heated capillary temperature, 250°C; ion selection threshold, 33.000 counts.

Thermo binary raw files were transformed either to mzXML files using msconvert (Proteowizard Tools proteowizard.sourceforge.net/tools.shtml) or mgf files using Proteome Discoverer 1.4-PostSearch Recalibrator Node (Thermo).

Cross-linked peptides were mapped using Crossfinder (Forné et al., 2012; Mueller-Planitz, 2015) Crossfinder allows but does not require the use of isotope-coded chemical cross-linkers. False discovery rates reported by Crossfinder are based on a target-decoy search strategy (Walzthoeni et al., 2012). An executable version for Windows 64-bit systems can be downloaded from our website. An MS1 and MS2 tolerance window of 18 and 25 ppm, respectively, was applied. The number of missed trypsin cleavage sites was set to two to three. For all peptides, oxidation of methionine was set as variable modification and carbamidomethylation of cysteine as fixed modification. Lysine residues were considered as cross-linking sites for BS^2G and BS^3, in accordance with the specificity of NHS esters to react with primary amines. All amino acid residues were considered as potential sites for UV-induced cross-linking of Bpa. Since cross-linking of lysine residues blocks tryptic digests at these sites (Holding, 2015), cross-link candidates with a C-terminal cross-linked lysine were excluded from the analysis. Cross-links spanning less than ten amino acids were also removed from the downstream analysis.

Results were filtered in Crossfinder according the following parameters for identification of cross-linking candidates: False-discovery rate (FDR) ≤ 0.05, number of fragment ions per spectrum ≥ 5, number of fragment ions per peptide ≥ 2, fractional intensity of assigned MS2 peaks ≥ 0.05, relative filter score: 100. Cross-links identified in the respective negative controls, i.e. the unirradiated $ISWI_{M578B}$ and $ISWI_{H483B}$ proteins and DMSO-treated $ISWI_{WT}$ samples, were also automatically filtered out. MS2 spectra of identified cross-links were further manually validated by assessing correct assignment of precursor and fragment ions. Medium- and high-confidence cross-links were used for the downstream analysis, whereas low-confidence cross-links (9.9% of all cross-links) were removed from the analysis.

Cross-links were considered reproduced if detected in less stringently filtered datasets (FDR ≤ 0.1). More specifically, we categorized each identified cross-link listed in Tables S1 and S2 in four reproducibility groups: "I", The identical cross-linked peptide was identified in an independent experiment; "II", The same pair of amino acids was cross-linked in an independent experiment; "III", The identical cross-linking sites were found in technical replicates, i.e, in another sample of the same experiment; "IV", not reproduced. By criteria I to III, we reproduced 82 of all 101 cross-linked peptides or 50 of 68 amino-acid connections, respectively.

SAXS

Protein samples for SAXS measurements were dialyzed against a buffer containing 50 mM Hepes-KOH pH 7.6, 1.5 mM $Mg(OAc)_2$, 0.2 mM KOAc, 10% glycerol, 1 mM DTT. Sample solutions were syringe filtered with 0.22 μm pore size (Merck Millipore, Germany) and centrifuged at 13500 rpm for 10 min in a tabletop centrifuge (Eppendorf, Germany) prior to each measurement. SAXS measurements were performed for at least three different protein concentrations for all protein constructs and conditions (1 to 4 mg/ml for $ISWI_{WT}$ and 1.5 to 7 mg/ml for $ISWI_{\Delta HSS}$). Scattering profiles collected at different protein concentrations were superimposable after rescaling by the intensity at zero angles, indicating that aggregation of the samples was minimal (Figure S1A).

SAXS measurements were performed at beamline BM29, ESRF, Grenoble (Pernot et al., 2013) at an X-ray wavelength λ of 0.99 Å, using a sample-to-detector distance of 2.87 m and a Pilatus 1M detector, resulting in an usable q-range of $\sim$ 0.1 to 3.5 nm^{-1} ($q = 4\pi \cdot \sin(\theta)/\lambda$, where θ is the total scattering angle). For each sample concentration, ten runs with an exposure time of 4 s in

'flow' mode were conducted at room temperature. Buffer samples were measured using identical procedures before and after each sample measurement. Sample and buffer data from each run were analyzed for radiation damage; no damage was observed in any of the measurements.

SAXS data processing was performed running custom-written MATLAB scripts (The MathWorks Inc., Natick, MA, USA). Matching sample and buffer profiles were averaged and buffer profiles were subtracted for background correction. For all samples, slight concentration effects in the low q-region could be observed for the highest sample concentration (Figure S1A). Thus, to obtain optimum data quality, we scaled and merged data from the lowest and highest sample concentration for the low- and high q-region, respectively.

We performed Guinier analyses based on a selfcustom-written MATLAB script to obtain radii of gyration (R_g) for all measured constructs, i.e. we fitted the logarithm of the scattering intensity as a function of q^2 to a straight line for small values of q (Guinier, 1939) (Figure S1B). Mean and standard deviations of the R_g values for each sample were computed from 10 R_g calculations that systematically varied the fitting range between $1.0 < q_{max} \cdot R_g < 1.3$. We used the program PRIMUS to compute the pair distance distribution function $P(r)$ (Konarev et al., 2003).

To reconstruct low-resolution density maps from the SAXS data, we used the program DAMMIF (Franke and Svergun, 2009). To determine a compact interconnected model whose scattering pattern fits the experimental data the software employs a simulated annealing protocol. For each scattering profile, 20 independent runs in the "slow" mode were performed with default parameters and assuming no symmetry. Next, the 20 models of each molecule were averaged using the program DAMAVER (Volkov and Svergun, 2003), which runs a sequence of programs: in a first step, the program aligns the low resolution models from DAMMIF based on their axes of inertia using a normalized spatial discrepancy (NSD) criterion (Kozin and Svergun, 2001), which provides a quantitative measure of similarity between different models. For identical objects, the NSD value is 0 and values exceeding 1 refer to objects that systematically differ from one another. For all constructs presented in this work, the independent reconstruction runs yielded structurally similar models as indicated by pairwise NSD values were in the range between zero and one. The aligned bead models were averaged and filtered by removing loosely connected beads. Aligned bead models were converted to electron density maps using the pdb2vol program from the SITUS package (version 2.7.2) (Wriggers et al., 1999). Finally, the models were aligned to the corresponding atomic structures (Berman et al., 2000), by minimizing the NSD value between both structures. Molecular graphics of the *ab initio* envelope models and corresponding atomistic structures were prepared using visual molecular dynamics (Humphrey et al., 1996).

Molecular Modeling

The input structures for computational modeling were prepared as followed. For building the ISWI ATPase structure, we first generated a homology model from the crystal structure of the yeast remodeler ScChd1 (pdb 3MWY) using MODELLER (Webb and Sali, 2016). Residues N- and C-terminal to residue 116 and 637, respectively, were deleted from the final model because they differed significantly between different experimental structures. The ATPase domain was cut at a computationally predicted hinge region (residues 351–352) (Emekli et al., 2008) connecting the two ATPase lobes. The two lobes used for docking therefore comprised residues 116–351 and 352–637.

To reconstruct the ISWI full-length protein architecture, we used the crystal structure of the HSS domain (pdb 1OFC) (Grune et al., 2003) and the ten best structural models of the ATPase domain in an ensemble docking approach.

The protein structures were converted into the ATTRACT coarse-grained (Fiorucci and Zacharias, 2010; Zacharias, 2003) and all-atom representation (Jorgensen and Tirado-Rives, 1988; Linge and Nilges, 1999) using the ATTRACT tools 'reduce' and 'aareduce'. Missing atoms were built with PDB2PQR (Dolinsky et al., 2004, 2007) and protonation states were determined by PropKa (Li et al., 2005).

Structural modeling was performed with the ATTRACT protein-protein docking approach (de Vries et al., 2015) using the cross-linking data as distance restraints. For each cross-linked residue pair, the distance between the Cα atoms was restrained by an upper harmonic potential with a maximum distance (d_{max}). The d_{max} were set to 25 Å and 29 Å for chemical BS^2G or BS^3 cross-links, respectively, comparable to previous studies (Fischer et al., 2013; Herzog et al., 2012; Leitner et al., 2012; Lossl et al., 2014). These values were derived by adding the length of lysine side chains, the length of the spacer (7.7 Å for BS^2G and 11.4 Å for BS^3) and a tolerance to account for flexibility (Merkley et al., 2014). For UV cross-links the d_{max} was estimated to be 20 Å, similar to published values (Taylor et al., 2014; Wittelsberger et al., 2006). For distances smaller than d_{max}, no penalty was applied. When modeling the ATPase domain, we employed an additional harmonic distance restraints between the C atom of residue 351 and the N atom of residue 352 (linker connectivity, d_{max} = 10 Å). During modeling, the protein domains were initially positioned at random positions and orientations. For the modeling of the ATPase structure, we used 100,000 starting configurations. For the full-length structure, we increased this number to 1,000,000 using 100,000 positions for each of the ten different ATPase structures in the ensemble. For each starting position, the center-of-mass translation and orientation of the protein partners was optimized in a potential energy minimization using the ATTRACT coarse-grained force field (Fiorucci and Zacharias, 2010; Zacharias, 2003) and the restraints derived from the cross-linking data. The internal structure of the domains was kept rigid during this large-scale search. The structures were then ranked by their ATTRACT score evaluated within a squared cutoff of 50 $Å^2$ and the restraint potentials. Finally, the top 200 structures were refined with the flexible interface refinement method iATTRACT (Schindler et al., 2015). The cross-linking distance restraints were also applied during the refinement stage.

We evaluated the convergence of the modeling by calculating the precision as the minimal average pair-wise Cα RMSD between all final 200 models (Schneidman-Duhovny et al., 2014). This yields a lower bound for the model error. The precision of the models was 3.4 Å and 3.3 Å for the DmATPase and the full-length DmISWI, respectively. After filtering using a cutoff χ-value of 1.3 for fits to the SAXS data, the precision values improved further to 2.3 Å (calculated over 62 models) and 1.4 Å (30 models). To further check for convergence in terms of sampling, we repeated the ATPase and full-length ISWI docking using a ten times larger number of starting positions. We obtained very similar results and no additional conformation could be observed (data not shown).

The docking models were compared against the SAXS data using FoXS with default settings and the reported reduced χ-values follow the standard convention implemented in FoXS (Schneidman-Duhovny et al., 2013. Control calculations with CRYSOL (Petoukhov et al., 2012)) gave identical results, within experimental error with default settings. All structures were visualized with PyMOL. All distances of cross-linked amino acids were measured with PyMOL and refer to the distances between the Cα atoms.

We reconstructed missing residues in ATPase and full-length DmISWI models against SAXS data using the software BUNCH (Petoukhov and Svergun, 2005). BUNCH was run in interactive mode. Input files required for BUNCH were generated using 'pre_bunch'. Required theoretical scattering patterns from subdomains were calculated using the program CRYSOL (Svergun et al., 1995). Requested parameters in BUNCH were set to default values, leaving the positions of the core domains of the ATPase domain (cf. Figure 2D) fixed. We used experimental scattering data from $ISWI_{\Delta HSS}$ and $ISWI_{WT}$ as input files for BUNCH.

DATA AND SOFTWARE AVAILABILITY

An executable version of Crossfinder for Windows machines (64-bit) is freely available from our website (http://www.molekularbiologie.abi.med.uni-muenchen.de/ueber_uns/mueller_planitz/publications/index.html) to academic users.